Polyhedron 54 (2013) 13–25

Contents lists available at SciVerse ScienceDirect

Polyhedron

journal homepage: www.elsevier.com/locate/poly

# A combined theoretical and experimental study of electronic structure and optical properties of β-$ZnMoO_4$ microcrystals

L.S. Cavalcante [a,b,*], E. Moraes [c], M.A.P. Almeida [c], C.J. Dalmaschio [c], N.C. Batista [b], J.A. Varela [a], E. Longo [a], M. Siu Li [d], J. Andrés [e], A. Beltrán [e]

[a] Universidade Estadual Paulista, P.O. Box 355, CEP 14801-907 Araraquara, SP, Brazil
[b] UESPI-CCN, Departamento de Química, Rua João Cabral, P.O. Box 2231, 64002-150, Teresina-PI, Brazil
[c] DQ-LIEC-Universidade Federal de São Carlos, P.O. Box 676, CEP 13565-905, São Carlos, SP, Brazil
[d] IFSC-Universidade de São Paulo, P.O. Box 369, 13560-970, São Carlos, SP, Brazil
[e] Department of Química-Física-Analítica, Universitat Juame I, 12071 Castello, Spain

ARTICLE INFO

*Article history:*
Received 14 July 2012
Accepted 4 February 2013
Available online 11 February 2013

*Keywords:*
$ZnMoO_4$
Raman
Defects
Band gap
DFT
Photoluminescence

ABSTRACT

In this paper, a combined theoretical and experimental study on the electronic structure and photoluminescence (PL) properties of beta zinc molybdate (β-$ZnMoO_4$) microcrystals synthesized by the hydrothermal method has been employed. These crystals were structurally characterized by X-ray diffraction (XRD), Rietveld refinement, Fourier transform Raman (FT-Raman) and Fourier transform infrared (FT-IR) spectroscopies. Their optical properties were investigated by ultraviolet–visible (UV–Vis) absorption spectroscopy and PL measurements. First-principles quantum mechanical calculations based on the density functional theory at the B3LYP level have been carried out. XRD patterns, Rietveld refinement, FT-Raman and FT-IR spectra showed that these crystals have a wolframite-type monoclinic structure. The Raman and IR frequencies experimental results are in reasonable agreement with theoretically calculated results. UV–Vis absorption measurements shows an optical band gap value of 3.17 eV, while the calculated band structure has a value of 3.22 eV. The density of states indicate that the main orbitals involved in the electronic structure of β-$ZnMoO_4$ crystals are (O 2*p*-valence band and Mo 4*d*-conduction band). Finally, PL properties of β-$ZnMoO_4$ crystals are explained by means of distortions effects in octahedral [$ZnO_6$] and [$MoO_6$] clusters and inhomogeneous electronic distribution into the lattice with the electron density map.



## 1. Introduction

Zinc molybdate ($ZnMoO_4$) crystals are semiconductor inorganic solids that exhibit two types of structures α-alpha and β-beta which can be obtained depending on synthesis conditions and processing time/temperature [1–3]. α-$ZnMoO_4$ crystals present a triclinic structure, space group $P\bar{1}$ and point group symmetry $C_1$ [4]. In the triclinic structure, zinc atoms are coordinated to six oxygens which form the distorted octahedral [$ZnO_6$] clusters while the molybdenum atoms are linked to four oxygens with its configuration of tetrahedral [$MoO_4$] clusters [5]. However, β-$ZnMoO_4$ crystals have a wolframite-type monoclinic structure, space group $P2/c$ and point group symmetry $C_{2h}^4$ [6]. In the monoclinic structure, the zinc and molybdenum atoms are surrounded by six oxygens which form the distorted octahedral [$ZnO_6$]/[$MoO_6$] clusters [6]. Both α- and β-$ZnMoO_4$ crystals in undoped and doped forms have been investigated because of their interesting electronic properties and high potential for possible industrial applications in various scientific fields such as: luminescence [7–9], red/green phosphors for light-emitting diodes [10–16], cryogenic/bolometric scintillating detectors [16–19], microwave dielectric [20], anticorrosive paints [21], cathode electrode in lithium batteries [22], photocatalyst for degradation of Victoria blue R and methyl orange dyes [23,24], and as a humidity sensor [25].

In the past years, $ZnMoO_4$ crystals with two types of α-triclinic and β-monoclinic structures were initially prepared by traditional methods such as: a oxide mixture or solid state reaction [26–30]. However, these preparation methods require high temperatures, long processing times and sophisticated equipment with high maintenance costs as well as the formation of deleterious phases. A possible alternative for the reduction of these problems and the production of these crystals at a low temperature can be the use of wet chemical methods such as coprecipitation controlled/calcination [31,32] and citrate complex precursors [33]. Recently, the hydrothermal (HT) method has attracted the attention of the

* Corresponding author at: Universidade Estadual Paulista, P.O. Box 355, CEP 14801-907 Araraquara, SP, Brazil. Tel.: +55 16 3361 8214, mobile: +55 86 9808 4129.
*E-mail address:* laeciosc@bol.com.br (L.S. Cavalcante).

0277-5387/$ - see front matter © 2013 Elsevier Ltd. All rights reserved.
http://dx.doi.org/10.1016/j.poly.2013.02.006

scientific community in the preparation of different molybdates with several sizes, shapes and nanostructures [34–36]. In particular, this synthesis method enables the attainment of pure molybdate at low temperatures (120–160 °C) in micro and nanoscale with excellent photoluminescence (PL) properties [37–41]. From a theoretical perspective, only one recent research [42] has been reported in the literature which shows band structure calculations and partial densities of states for the triclinic structure of α-$ZnMoO_4$ crystals using the full-potential linear-augmented-plane-wave method.

Therefore, in this work, we report the synthesis of β-$ZnMoO_4$ microcrystals by means of the HT method. These microcrystals were analyzed by X-ray diffraction (XRD), Fourier transform (FT-Raman), FT-Infrared (IR), ultraviolet–visible (UV–Vis) absorption spectroscopies and PL measurements. PL spectroscopy is an indispensable tool to elucidate electronic structure changes and physical phenomena involved in optical properties. In addition, we present first-principles quantum mechanical calculations based on the density functional theory (DFT) to find a correlation between experimental results of Raman/IR spectroscopies and the Raman/IR-active frequencies theoretical, band gap and PL properties of β-$ZnMoO_4$ microcrystals with a monoclinic structure.

## 2. Experimental details

### 2.1. Synthesis of β-$ZnMoO_4$ microcrystals

β-$ZnMoO_4$ microcrystals were prepared by the HT method at 140 °C for 8 h. The typical synthesis procedure for these microcrystals is described as follows: 2.5 mmol or 0.6079 g of molybdate (VI) sodium dihydrate [$Na_2MoO_4{\cdot}2H_2O$] (99.5% purity, Sigma-Aldrich) and 2.5 mmol or 0.7512 g of zinc(II) nitrate hexahydrate [$Zn(NO_3)_2{\cdot}6H_2O$] (99% purity, Sigma-Aldrich) were dissolved separately in two plastic vessels (Falcon) with a capacity of 50 mL of deionized water. After dissolution of these salts at room temperature. Then the first solution (50 mL) with ($Na^+$ and $MoO_4^{2-}$ ions) and the second solution (50 mL) with the ($Zn^{2+}$ and $NO_3^-$ ions) were mixed and transferred into a stainless-steel autoclave. This system was kept under constant agitation during the total time on the synthesis HT. The HT processing promotes favorable conditions for chemical reactions between the $Zn^{2+}$ and $MoO_4^{2-}$ ions which results in the formation of crystalline β-$ZnMoO_4$ microcrystals as shown in Eq. (1) below:

$$2Na^+_{(aq)} + MoO^{2-}_{4(aq)} + 2H_2O + Zn^{2+}_{(aq)} + 2NO^-_{3(aq)} + 6H_2O \overset{\approx(140^\circ C/8h)\approx}{\rightarrow} \beta\text{-}ZnMoO_{4(s)} + 2Na^+_{(aq)} + 2NO^-_{3(aq)} + 8H_2O \quad (1)$$

Then the stainless-steel autoclave was cooled to room temperature. The resulting suspensions were washed several times with deionized water to remove residual $Na^+$ ions. Finally, crystalline β-$ZnMoO_4$ precipitated powders of a light-gray color were collected and dried on a hot plate at 70 °C for 8 h.

### 2.2. Characterizations of β-$ZnMoO_4$ microcrystals

These β-$ZnMoO_4$ microcrystals were structurally characterized by X-ray diffraction (XRD) patterns using a D/Max-2500PC diffractometer Rigaku (Japan) with Cu-Kα radiation ($\lambda$ = 1.5406 Å) in the $2\theta$ range from 10° to 73° in normal routine with a scanning velocity of 2°/min and from 10° to 75° with a scanning velocity of 1°/min in the Rietveld routine. FT-Raman spectroscopy was recorded with a Bruker-RFS 100 (Germany). The Raman spectrum from 50 to 1000 $cm^{-1}$ was obtained using a 1064 nm line with a Nd:YAG laser kept at its maximum output power at 100 mW and counts of 500 scans. FT-IR spectroscopy was performed in a Bomem–Michelson spectrophotometer in the transmittance mode (model MB-102). The FT-IR spectrum in the range from 200 to 1050 $cm^{-1}$ was obtained using KBr pellets as a reference. The shapes of these β-$ZnMoO_4$ microcrystals were observed with a field emission scanning electron microscopy model Inspect F50 (FEI Company, Hillsboro, USA) operated at 15 kV. UV–Vis spectra were taken using a Varian spectrophotometer (Model Cary 5G, USA) in a diffuse reflectance mode. PL measurements were performed through a Monospec 27 monochromator (Thermal Jarrel Ash, USA) coupled to a R446 photomultiplier (Hamamatsu Photonics, Japan). A krypton ion laser (Coherent Innova 90K, USA) ($\lambda$ = 350 nm) was used as the excitation source; its maximum output power was maintained at 500 mW. The laser beam was passed through an optical chopper, and its maximum power on the sample was maintained at 40 mW. PL measurements were performed at room temperature.

### 2.3. Computational method and periodic model of β-$ZnMoO_4$ microcrystals

All the calculations were carried out with the CRYSTAL09 computer program [43] within the framework of the density functional theory with the hybrid functional B3LYP [44,45]. The calculations were performed using a periodically repeating geometry; the method is described in the CRYSTAL09 manual [43]. Zn, Mo, and O atoms centers are described in basis sets: 86-411d31G, PS-311(d31)G and 8-411G, respectively, taken from the Crystal web site [46] where PS stands for Hay & Wadt's nonrelativistic small core pseudopotential [47]. The diagonalization of the Fock matrix was performed at adequate *k*-point grids in the reciprocal space which is the Pack-Monkhorst/Gilat shrinking factor IS = ISP = 4. The thresholds controlling the accuracy of the calculation of Coulomb and exchange integrals were set to $10^{-8}$ (ITOL1 to ITOL4) and $10^{-14}$ (ITOL5) which assures a convergence in total energy better than $10^{-7}$ a.u. whereas the percentage of Fock/Kohn–Sham matrix mixing was set to 40 (IPMIX = 40) [47]. Full optimization of the (*a*, *b*, *c*) lattice parameters as well as the (*x*, *y*, *z*) internal coordinates has been carried out. The XCRYSDEN program version 1.5.23 [48] has been used to draw the band structure diagram, density of states (DOS) and the maps of the electronic density. The Raman/IR vibrational modes and their corresponding frequencies were calculated using numerical second derivatives of the total energies as implemented in the CRYSTAL09 package [43].

## 3. Results and discussion

### 3.1. X-ray diffraction and Rietveld refinement analyses of β-$ZnMoO_4$ crystals

Fig. 1(a–c) show the experimental XRD patterns and Rietveld refinement plot of β-$ZnMoO_4$ microcrystals synthesized at 140 °C for 8 h by the HT method and theoretical XRD profile with their specific lines position of optimized monoclinic structure, respectively.

According to the XRD patterns analysis illustrated in Fig. 1(a), all XRD peaks can be indexed perfectly to a wolframite-type monoclinic structure with the space group *P*2/*c* and point group symmetry $C^4_{2h}$. Moreover, XRD patterns are in agreement with the respective Joint Committee on Powder Diffraction Standards (JCPDS) Card No. 25-1024 [49] and theoretical results. The profile of the all XRD peaks are narrower, that indicate the presence of large crystals with a considerable degree of structural order at long-range. The experimental lattice parameters, unit cell volume and atomic positions of β-$ZnMoO_4$ microcrystals were calculated

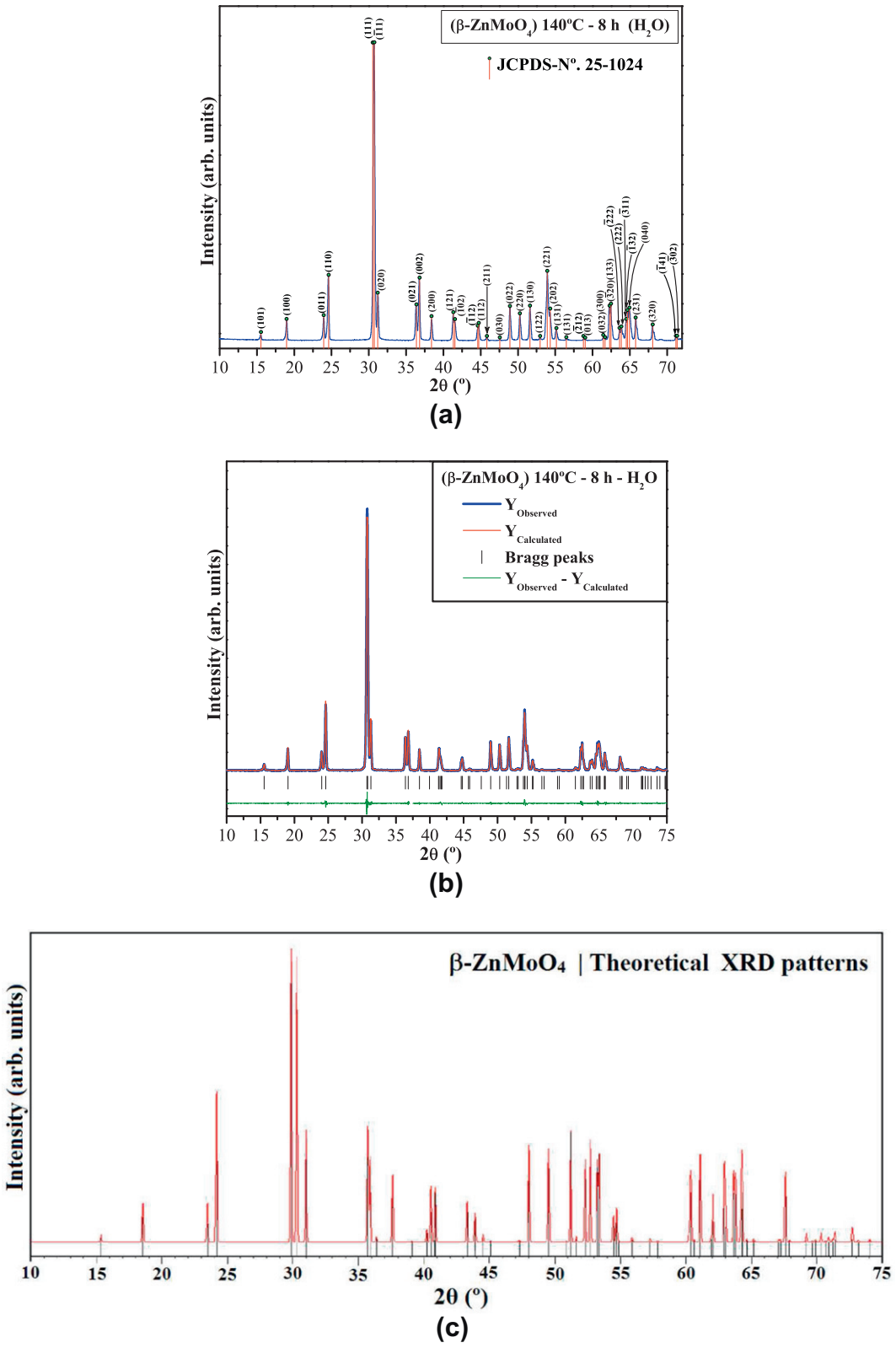


**Fig. 1.** (a) XRD patterns, (b) Rietveld refinement plot of β-$ZnMoO_4$ microcrystals synthesized at 140 °C for 8 h in HT system and (c) XRD patterns theoretically calculated, respectively.

using the Rietveld refinement method [50] with the Maud program (version 2.33) [51,52] (Fig. 1(b)). The experimental results obtained from Rietveld refinement were optimized by theoretical calculations. The theoretical lattice parameters and atomic positions were used to model theoretical XRD profile with their specific lines position (Fig. 1(c)). The experimentally obtained data from Rietveld refinement and theoretical calculations, respectively, are shown in Table 1.

**Table 1**
Lattice parameters, unit cell volume, atomic coordinate obtained experimentally from the structural refinement by the Rietveld method and theoretically calculated from DFT method.

| (a) ■ Atoms[a] | Wycroff | Site | S.O.F. | *x* | *y* | *z* |
|---|---|---|---|---|---|---|
| Zn | 2*f* | 2 | 1 | 0.5 | 0.68588 | 0.25 |
| Mo | 2*e* | 2 | 1 | 0 | 0.19564 | 0.25 |
| O1 | 4*g* | 1 | 1 | 0.23115 | 0.35436 | 0.31255 |
| O2 | 4*g* | 1 | 1 | 0.21435 | 0.93315 | 0.32451 |
| $a$ = 4.6987(3) Å, $b$ = 5.7487(2) Å; $c$ = 4.9044(2) Å; $V$ = 132.47 Å$^3$; β = 90.3312°; $R_w$ = 6.54%; $R_{wnb}$ = 5.67%; $R_b$ = 4.23%; $R_{exp}$ = 3.23% and s = 2.02 | | | | | | |
| (b)★ Atoms[b] | | | | | | |
| Zn | 2*f* | 2 | 1 | 0.5 | 0.67568 | 0.25 |
| Mo | 2*e* | 2 | 1 | 0 | 0.18603 | 0.25 |
| O1 | 4*g* | 1 | 1 | 0.26110 | 0.38081 | 0.39073 |
| O2 | 4*g* | 1 | 1 | 0.21320 | 0.89251 | 0.42669 |
| $a$ = 4.7391 Å, $b$ = 5.8100 Å; $c$ = 5.0895 Å; β = 90.6470° and $V$ = 140.12 Å$^3$ | | | | | | |

S.O.F., site occupancy factor.
[a] β-$ZnMoO_4$ microcrystals synthesized at 140 °C for 8 h by HT method.
[b] Theoretical results.

In this table, it was verified that the lattice parameters and unit cell volumes of a monoclinic structure are very close to the values recently published in the literature [3]. Small variations between these values can be related to the peculiarity of each synthesis method where the experimental variables (temperature, time processing, heating rate, solvents, etc.) are able to influence the organization of the octahedral [$ZnO_6$] and [$MoO_6$] clusters within the monoclinic structure. Also, these variables cause the formation or reduction of structural defects (oxygen vacancies, distortion on the bonds, stresses and strains on the crystalline lattice). Moreover, in this table, the fit parameters ($R_{wnb}$, $R_b$, $R_{exp}$, $R_w$, and $\sigma$) suggest that the refinement results are quite reliable. It is interesting to note that there are considerable variations in the atomic positions related to the oxygen atoms while zinc and molybdenum atoms practically keep their positions fixed within the structure. These results indicate the existence of distortions on the octahedral [$ZnO_6$] and [$MoO_6$] clusters presents in electronic structure of β-$ZnMoO_4$ microcrystals.

### 3.2. Unit cell representations of β-$ZnMoO_4$ crystals

Figs. 2(a, c and e) illustrate the representations of experimental β-$ZnMoO_4$ unit cells and Figs. 2(b, d and f) shows the representations of theoretical β-$ZnMoO_4$ unit cells in same perspective, respectively.

The lattice parameters and atomic positions obtained from the Rietveld refinement and theoretical calculations presented in Table 1 were used to model these unit cells using the Visualization for Electronic and Structural Analysis (VESTA) program, version 3.1.2, for Windows [53]. The monoclinic structure of the β-$ZnMoO_4$ crystals is characterized by exhibiting a space group $P2/c$, point-group symmetry $C_{2h}^4$ and two clusters per unit cell ($Z$ = 2). In these unit cells, the Zn and Mo atoms are coordinated to six oxygens atoms which form the distorted octahedral [$ZnO_6$] and [$MoO_6$] clusters (6-vertices, 6-faces, and 12-edges) [54]. As it can be observed, that the Figs. 2(a and b); (c and d); and (e and f) exhibits small differences in (O–Zn–O) and (O–Mo–O) bond angles. However, the experimental β-$ZnMoO_4$ crystals present minor unit cell volume and major distortions on the octahedral [$ZnO_6$]/[$MoO_6$] clusters in relation to unit cell of theoretical β-$ZnMoO_4$ crystal lattice. In principle, this phenomenon occurs due to experimental conditions required for crystallization and formation of β-$ZnMoO_4$ crystals and other phenomena involved such as dissolution and recrystallization mechanisms under HT conditions [55]. These small differences between the experimental and theoretical β-$ZnMoO_4$ unit cells can be noted in Figs. 2(a–f).

### 3.3. Fourier-transform Raman/infrared spectroscopies: theoretical and experimental analyses of β-$ZnMoO_4$ crystals

According to the group theory calculations and symmetry [56–58], molybdate and tungstate crystals with a wolframite-type monoclinic structure present $3N$ = 36 degrees of freedom. Therefore, there are $N$ = 12 atoms within the unit monoclinic cell as illustrated previously (see Fig. 3(a and b)). In our case, β-$ZnMoO_4$ microcrystals have 36 distinct vibrational modes (Raman and infrared) as indicated in Eq. (2) [57,58]:

$$\Gamma_{(\text{Raman+Infrared})} = 8A_g + 10B_g + 8A_u + 10B_u \quad (2)$$

where the $A_g$ and $B_g$ are Raman-active modes, and $A_u$ and $B_u$ are active vibrational modes in the infrared spectrum; the $A$ and $B$ modes are nondegenerate. The terms "$_g$ and $_u$" subscripts indicate the parity under inversion in centrosymmetric β-$ZnMoO_4$ crystals. Therefore, only 18 active vibrational modes are expected in Raman spectra of β-$ZnMoO_4$ crystals as represented by Eq. (3) below [59]:

$$\Gamma_{(\text{Raman})} = 8A_g + 10B_g \quad (3)$$

According to the literature [60,61] and the data obtained from the structural refinement of the β-$ZnMoO_4$ crystals with a wolframite-type monoclinic structure, these crystals have only distorted octahedral [$ZnO_6$] and [$MoO_6$] clusters with a symmetry group $O_h$, space group $P2/c$ and symmetry site $C_2$. Raman spectra of β-$ZnMoO_4$ crystals can be classified into two types of groups (external and internal modes). External vibrational modes are related to the lattice phonons which corresponds to the motion of distorted octahedral [$ZnO_6$] clusters in the unit cell. The internal vibrational modes are ascribed to vibrations of distorted octahedral [$MoO_6$] clusters by assuming a center of mass of the steady state. The distorted octahedral [$MoO_6$] clusters have their vibrations composed by six internal modes (four $A_g$ and two $B_g$). The other vibrational modes with low values in Raman spectra are external modes.

Figs. 3(a and b) illustrate the FT-Raman spectrum and specific theoretical/experimental Raman modes of β-$ZnMoO_4$ microcrystals, respectively.

In Fig. 3(a), we can identify 18 Raman active vibrational modes between 50 and 1000 cm$^{-1}$ for β-$ZnMoO_4$ microcrystals synthesized at 140 °C for 8 h by the HT method. The main Raman ($A_g$) mode referent to intense peak located at around 878 cm$^{-1}$ is assigned to the symmetric stretch of bonds (←O←Mo→O→) (see inset Fig. 3(a)). Moreover, two Raman ($A_g$ and $B_g$) modes at approximately (778 cm$^{-1}$ and 701 cm$^{-1}$) are assigned to the asymmetric stretch of bonds (→O→Mo→O→) [62] (see inset Fig. 3(a))

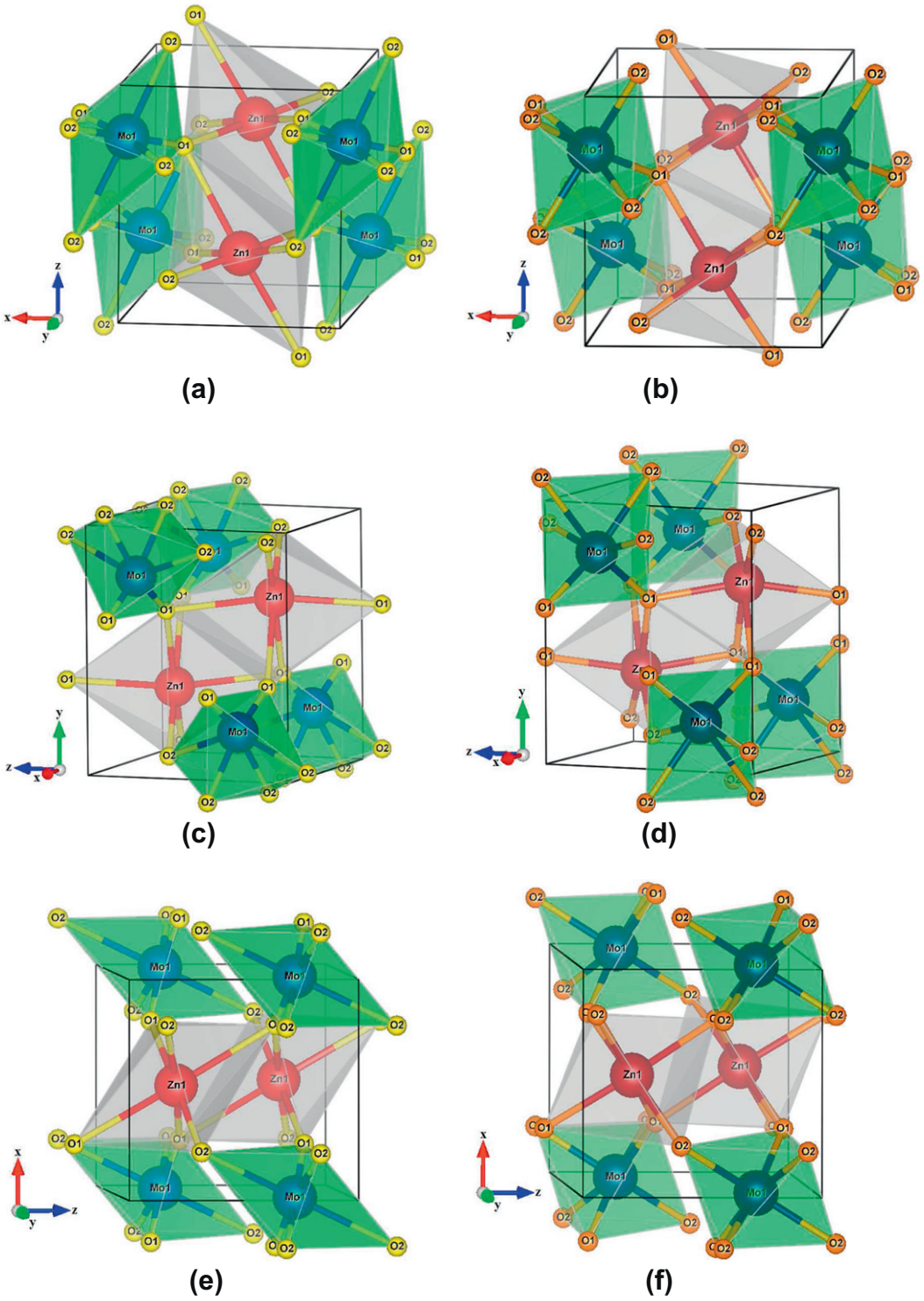


**Fig. 2.** Schematic representation of the monoclinic unit cells corresponding to β-$ZnMoO_4$ crystals projected at same axis: (a, c and e) experimental and (b, d and f) theoretical, respectively.

while a Raman ($B_g$) mode of low intensity at around 191 $cm^{-1}$ is ascribed to the symmetric stretch of bonds (←O←Zn→O→) (see inset Fig. 3(a)) [63]. Therefore, all Raman peaks correspond to a wolframite-type monoclinic structure. The experimental positions of 18 Raman vibrational modes were identified (●) and compared with those Raman-active modes calculated theoretically (∗) through atomic positions and lattice parameters for the optimized β-$ZnMoO_4$ crystal (see Fig. 3(b)) and their respective experimental and theoretical positions are listed in the Supplementary data (Table S1).

In Fig. 3(b), there is good agreement between the Raman-active modes of β-$ZnMoO_4$ microcrystals synthesized experimentally and theoretically obtained from *ab-initio* calculations. Some small variations in the typical positions of the vibrational modes can be

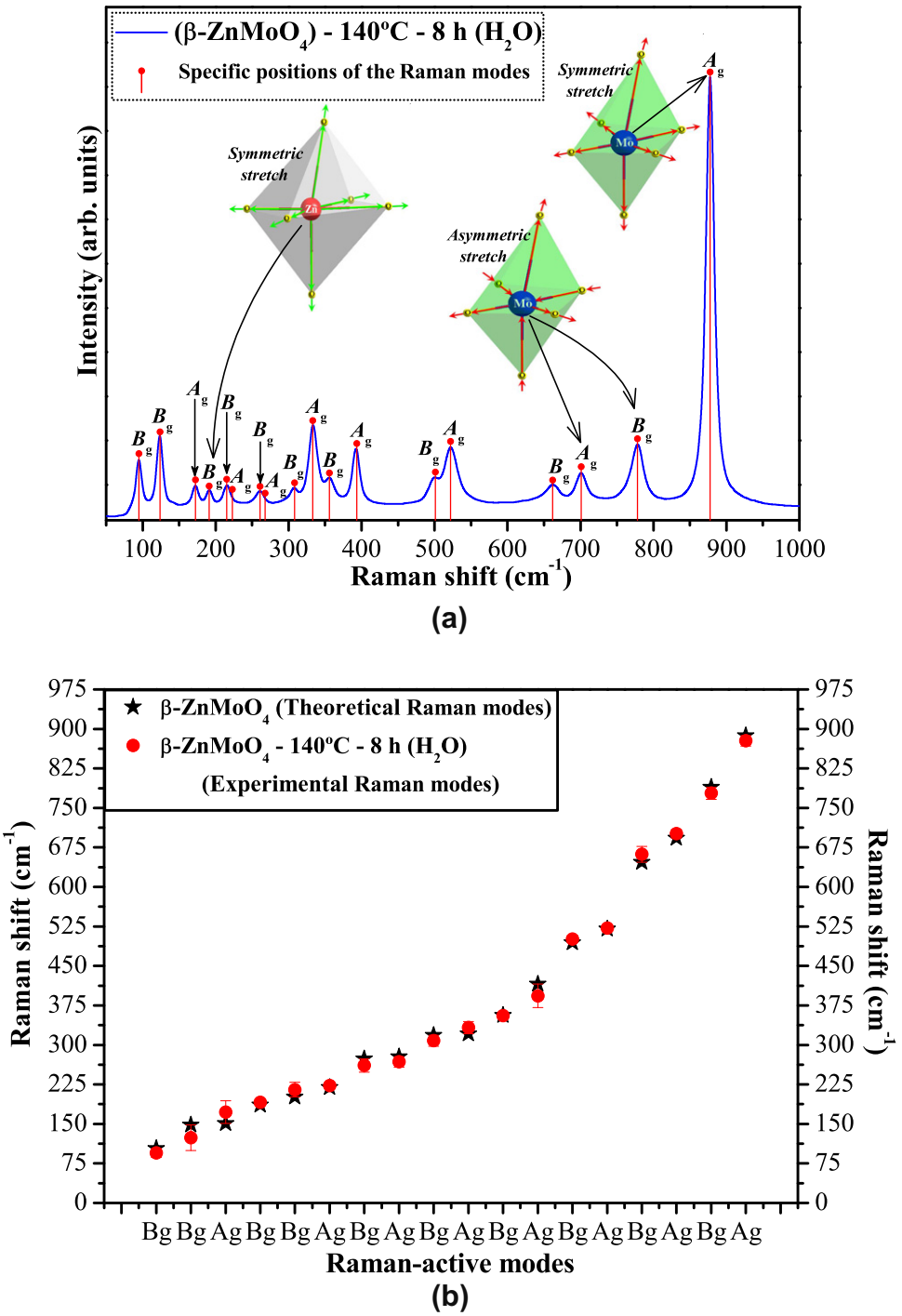


**Fig. 3.** (a) FT-Raman spectrum of β-$ZnMoO_4$ microcrystals synthesized at 140 °C for 8 h in HT system and (b) comparative between the relative positions of theoretical and experimental Raman-active modes.

caused by preparation methods, average crystal size, distortions on the (O–Zn–O)/(O–Mo–O) bonds, internal forces interactions between the [$ZnO_6$]–[$MoO_6$]–[$ZnO_6$] clusters and/or different degrees of structural order-disorder within the lattice. Moreover, our theoretical calculation does not consider the non-harmonic contribution to the lattice vibrations.

As described earlier, Raman and infrared spectra display 34 different vibrational modes that were presented in Eq. (2). Only some of these modes are active in the infrared spectrum. Therefore, only 18 vibrational modes are expected in the infrared spectrum of β-$ZnMoO_4$ crystals, as represented by Eq. (4) below:

$$\Gamma_{(\text{Infrared})} = 8A_u + 10B_u \quad (4)$$

However, three modes ($1A_u$ and $2B_u$) are only acoustic vibrations and cannot be detected in the infrared spectrum. Therefore, the Eq. (4) should be reduced and can be better represented by Eq. (5) [64–66]:

$$\Gamma_{(\text{Infrared})} = 7A_u + 8B_u \quad (5)$$

In general, infrared (IR) spectroscopy elucidates the different types of vibrational modes between the atoms and their inter-atomic bonds in molybdates [67].

Figs. 4(a and b) illustrate the FT-IR spectrum and specific theoretical/experimental infrared modes of β-$ZnMoO_4$ microcrystals, respectively.

In Fig. 4(a) shows eight infrared-active vibrational modes between 200 and 1050 $cm^{-1}$ for β-$ZnMoO_4$ microcrystals synthesized at 140 °C for 8 h by the HT method. A very narrow band at around 257 $cm^{-1}$ is due to the ($B_u$) mode with the anti-symmetric stretch of bonds and interaction forces between the $[ZnO_6] \leftrightarrow [ZnO_6]$ clusters. Thus, two ($A_u$) modes at approximately 326 and 359 $cm^{-1}$ are related to the symmetric stretch (O←Zn←O→Zn→O) of the distorted octahedral $[ZnO_6]$–$[ZnO_6]$ clusters in a chain. The $A_u$ mode at around (410 $cm^{-1}$) is ascribed to an anti-symmetric stretch (→O→Zn→O→) of distorted octahedral $[ZnO_6]$ clusters. Two bands at approximately 453 and 516 $cm^{-1}$ are assigned to $B_u$ and $A_u$ modes which are related to the anti-asymmetric stretch (O←Mo←O←Mo←O) of distorted octahedral $[MoO_6]$–$[MoO_6]$ clusters in a chain. A broad band at around 665 $cm^{-1}$ corresponds to an $A_u$ mode which is the main band in the infrared spectrum of β-$ZnMoO_4$ crystals (see inset Fig. 4(a)) with distorted octahedral $[MoO_6]$ clusters which are assigned to an anti-symmetric stretching.

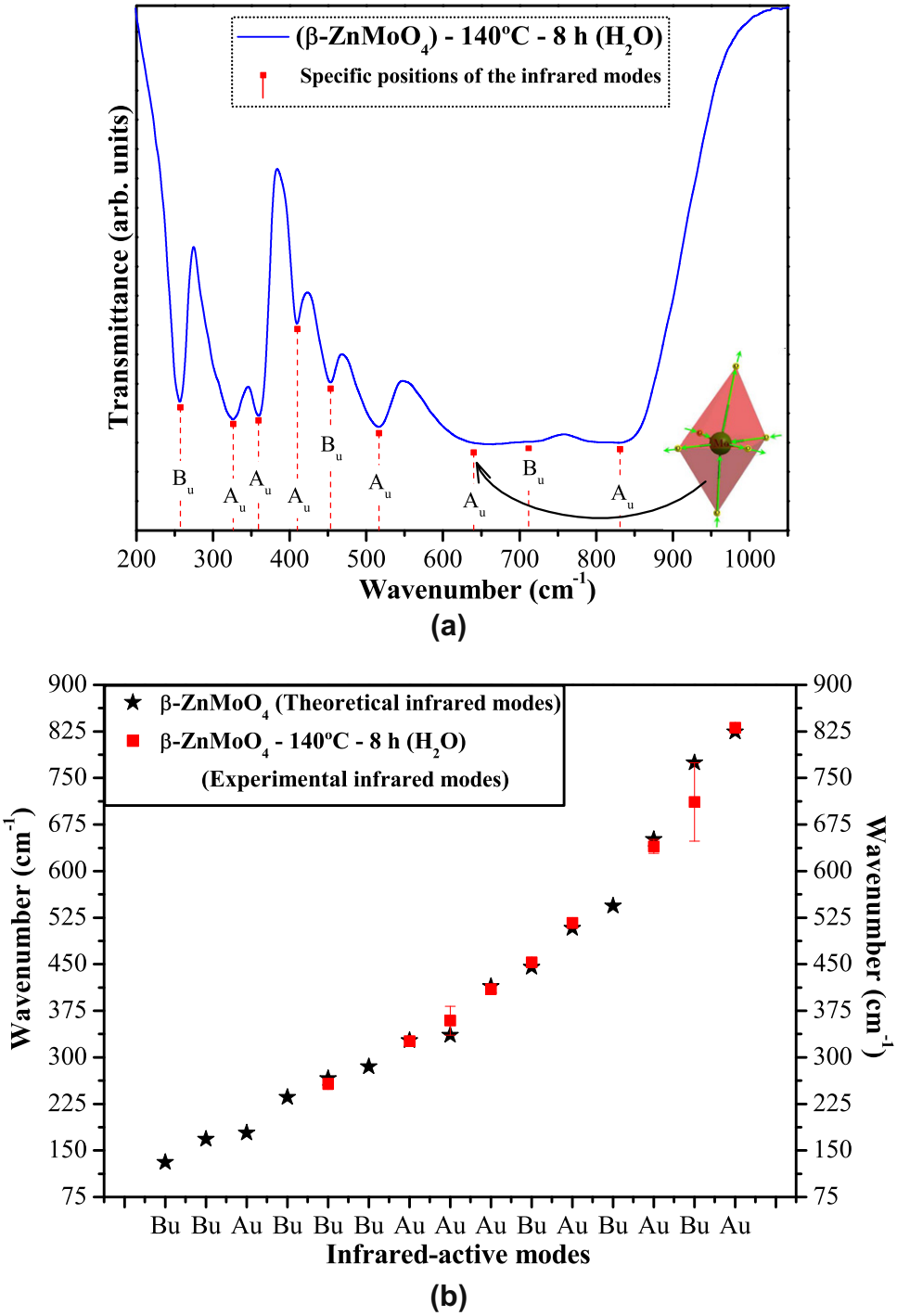


**Fig. 4.** (a) FT-IR spectrum of β-$ZnMoO_4$ microcrystals synthesized at 140 °C for 8 h in HT system and (b) comparative between the relative positions of theoretical and experimental IR-active modes.

Also, a shoulder at 712 $cm^{-1}$ is related to the $B_u$ mode. Finally, the band at around 829 $cm^{-1}$ is related to $A_u$ mode which is assigned to symmetric stretch (←O←Mo→O→) of the distorted octahedral [$MoO_6$] clusters. Typical theoretical (∗) and experimental positions (■) of IR-actives modes are shown in Fig. 4(b). Moreover, their respective experimental and theoretical values are listed in Supplementary data (Table S2).

Fig. 4(b) indicates a good conformity between the wavenumbers of the infrared-active modes which are experimentally determined and theoretically calculated. Moreover, theoretical results the evidence the presence of more some ($B_g$ and $A_g$) modes at 131.17 $cm^{-1}$, 168.42 $cm^{-1}$, 178.3 $cm^{-1}$, 236.03 $cm^{-1}$, 285.26 $cm^{-1}$ and 544.19 $cm^{-1}$ which were not experimentally detected due to the low detection limit imposed by the FT-IR spectrophotometer. In terms of spectral positions, small deviations in the IR-active modes of β-$ZnMoO_4$ microcrystals can be attributed to different degrees of interaction and modification on the O–Zn–O and O–Mo–O bond lengths and/or angles within the distorted octahedral [$ZnO_6$] and [$MoO_6$] clusters. We have noted that some of these infrared vibrational modes of β-$ZnMoO_4$ microcrystals are similar to isostructural $ZnWO_4$ crystals [68,69].

### 3.4. Ultraviolet–visible absorption spectroscopy and band structures of β-$ZnMoO_4$ crystals

The optical band gap energy ($E_{gap}$) was calculated by the method proposed by Kubelka and Munk [70]. This methodology is based on the transformation of diffuse reflectance measurements to estimate $E_{gap}$ values with good accuracy within the limits of assumptions when modeled in three dimensions [71]. Particularly, it is useful in limited cases of an infinitely thick sample layer. The Kubelka–Munk equation for any wavelength is described by Eq. (6):

$$F(R_\infty) = \frac{(1-R_\infty)^2}{2R_\infty} = \frac{k}{s} \tag{6}$$

where $F(R_\infty)$ is the Kubelka–Munk function or absolute reflectance of the sample. In our case, magnesium oxide (MgO) was the standard sample in reflectance measurements. $R_\infty = R_{sample}/R_{MgO}$ ($R_\infty$ is the reflectance when the sample is infinitely thick), $k$ is the molar absorption coefficient and $s$ is the scattering coefficient. In a parabolic band structure, the optical band gap and absorption coefficient of semiconductor oxides [72] can be calculated by Eq. (7):

$$\alpha h\nu = C_1(h\nu - E_{gap})^n, \tag{7}$$

where α is the linear absorption coefficient of the material, $h\nu$ is the photon energy, $C_1$ is a proportionality constant, $E_{gap}$ is the optical band gap and $n$ is a constant associated with different kinds of electronic transitions ($n = 0.5$ for a direct allowed, $n = 2$ for an indirect allowed, $n = 1.5$ for a direct forbidden and $n = 3$ for an indirect forbidden). According to the literature [73–75], the isostructural $ZnWO_4$ crystals exhibit an optical absorption spectrum governed by direct electronic transitions. In this phenomenon, after the electronic absorption process, the electrons located in the maximum-energy states in the valence band revert to minimum-energy states in the conduction band under the same point in the Brillouin zone [75,76]. Based on this information, $E_{gap}$ values of β-$ZnMoO_4$ crystals were calculated using $n = 0.5$ in Eq. (7): Finally, using the remission function described in Eq. (6) and with the term $k = 2\alpha$, we obtain the modified Kubelka–Munk equation as indicated in Eq. (8):

$$[F(R_\infty)h\nu]^2 = C_2(h\nu - E_{gap}), \tag{8}$$

Therefore, finding the $F(R_\infty)$ value from Eq. (8) and plotting a graph of $[F(R_\infty)h\nu]^2$ against $h\nu$, the $E_{gap}$ of β-$ZnMoO_4$ microcrystals was determined.

Figs. 5(a and b) illustrate the UV–Vis spectrum of β-$ZnMoO_4$ microcrystals synthesized at 140 °C for 8 h by HT method and their band structure, respectively.

The profile of the UV–Vis spectrum for β-$ZnMoO_4$ microcrystals indicates a typical optical behavior of structurally ordered crystalline materials. This microcrystal exhibits a direct $E_{gap}$ value of 3.17 eV (see Fig. 5(a)). Fig. 5(b) reveals that band structures of β-$ZnMoO_4$ crystals are characterized by well defined direct electronic transitions; i.e., the top of the valence band (VB) as well as the bottom of the conduction band (CB) are at the same Y ↔ Y (0, 0.5, 0) point. Therefore, was verified that theoretical band gap values ($E_{gap}$ = 3.22 eV) are close to values experimentally estimated by UV–Vis spectra (Fig. 5(a)).

### 3.5. Density of states of β-$ZnMoO_4$ crystals

Figs. 6(a and b) illustrate the DOS projected over the most important orbitals of the O and Mo atoms and the total DOS projected over all atoms involved in the electronic structure of β-$ZnMoO_4$ crystals, respectively.

Fig. 6(a) shows that the top of the VB are composed mainly of O ($2p_x$, $2p_y$, and $2p_z$ atomic orbitals) that connect with both Zn and Mo atoms. The lower part of the CB is formed mainly by Mo ($4d_{xy}$, $4d_{xz}$ and $4d_{yz}$, $4d_{x^2-z^2}$ and $4d_{z^2}$ atomic orbitals). In addition, was verified a slight contribution of the O 2$p$ orbitals. In an octahedral field, the 4$d$ orbitals of the Mo atoms are not degenerate; they first split in the $t_{2g}$ ($4d_{xy}$, $4d_{xz}$, and $4d_{yz}$) and $e_g$ ($4d_{x^2-z^2}$ and $4d_{z^2}$) orbitals. The $e_g$ orbitals have lobes that point at the oxygen ligands and thus will ascend in energy; the $t_{2g}$ orbitals have lobes that lie between ligands and thus will descend in energy (in the VB), but due to the distortion in octahedral [$MoO_6$] clusters, they present five different energies. The order of energies are opposite in the virtual bands so the most important contributions in the lower part of the CB are due to $e_g$ orbitals followed by $4d_{yz}$ ($t_{2g}$) and to a lesser extent, to the ($4d_{xy}$ and $4d_{xz}$) orbitals (see Figs. 6(a,b) lists the total DOS of all orbitals for β-$ZnMoO_4$ crystals. This total DOS shows that Zn atomic orbitals have a minimal contribution (between – 8 and 4 eV) due to a weak hybridization between the Zn and O orbitals. On the other hand, the total DOS indicates a strong hybridization between O 2$p$ (above the VB) and Mo 4$d$ orbitals (near the CB), respectively. Therefore, this analysis performed on the total orbital-resolved DOS denotes a significant dependence of Mo (4$d$) orbitals in the CB. In general, this behavior can be correlated with distortions on the octahedral [$MoO_6$] clusters within the monoclinic structure which are responsible for the origin of intermediary energy levels located above the CB.

### 3.6. Electron density maps and PL emission of β-$ZnMoO_4$ crystals

Figs. 7(a–d) show electron density maps performed on the Zn, Mo, O atoms and Zn–Mo atoms in different planes. Fig. 7(e) shows the possible mechanism of charge transference between the [$ZnO_6$]–[$MoO_6$]/[$ZnO_6$]–[$ZnO_6$] clusters involved in a monoclinic structure and Fig. 7(f) shows the PL behavior of β-$ZnMoO_4$ microcrystals synthesized at 140 °C for 8 h by the HT method, respectively.

Fig. 7(a) shows the electronic density map on the Zn atoms in (200) plane of β-$ZnMoO_4$ crystals. The regions in dark blue can be ascribed to a high electronic density or the number of electrons ($e'$) located in Zn atoms and between the [$ZnO_6$]–[$ZnO_6$] clusters while the region in red indicates the possible absence of the $e'$ between the [$ZnO_6$]–[$MoO_6$]–[$ZnO_6$] clusters. Moreover, we can verify that these regions have a value near zero which is donated in internal scale (see inset Fig. 7(a)). Regions with medium electronic density (in light blue) are possibly related to O atoms which are bonded to Zn atoms. Fig. 7(b) depicts the electronic density map

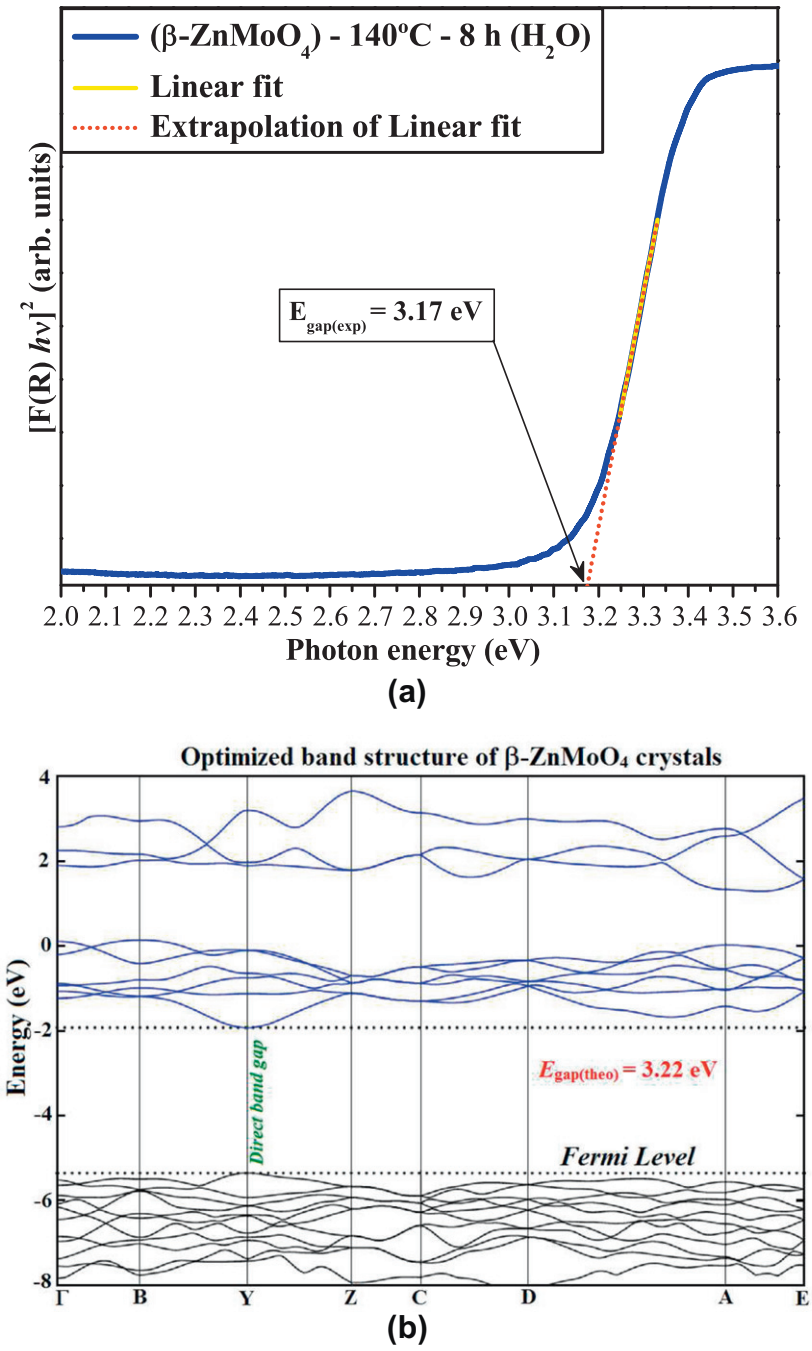


**Fig. 5.** (a) UV–Vis spectra of β-$ZnMoO_4$ microcrystals synthesized at 140 °C for 8 h in HT system and (b) optimized band structure of β-$ZnMoO_4$ crystals.

on Mo atoms in the (100) plane of β-$ZnMoO_4$ crystals. Regions in dark blue and light blue indicate a high electronic density for Mo atoms while the region in red indicates the absence of an electronic density between the [$MoO_6$]–[$ZnO_6$]–[$MoO_6$] clusters. In addition, was verified that these regions have a value near zero which is donated in internal scale (see inset Fig. 7(b)). In addition, circular green regions can possibly be related to O atoms bonded with Mo atoms. Fig. 7(c) illustrates the electronic density map on the O atoms in the (400) plane of β-$ZnMoO_4$ crystals. In this plane, a high electronic density corresponding to O atoms in circular blue and green regions can be verified. However, the O atoms are not equidistant due to distortions of the bonds present in octahedral on [$MoO_6$] and [$ZnO_6$] clusters which is in good agreement with models shown in Fig. 2(a–f). Based on this information, it is possible to confirm that 2*p* orbitals of O atoms are hybridized with $4d_{x^2-z^2}$ and $4d_{z^2}$ orbitals of Mo atoms are located on the axes in base of octahedron and apex of octahedron non-formed angles of 90°. Fig. 7(d) illustrates the electronic density map on the Zn and Mo atoms in the (004) plane of β-$ZnMoO_4$ crystals. In this figure can be confirmed that two Mo atoms are interconnected to one O atom with a high electronic density. Thus, the Zn atom is equidistant to two Mo atoms, and the region in different colors indicates that there is an inhomogeneous electron distribution and charges between distorted octahedral [$MoO_6$] and [$ZnO_6$] clusters.

Fig. 7(e) shows the laser employed in the excitation of β-$ZnMoO_4$ microcrystals. The wavelength energy (350 nm ≈3.543 eV) is able to excite several electrons localized in intermediary energy levels within the band gap (see Fig. 5(a)). These direct

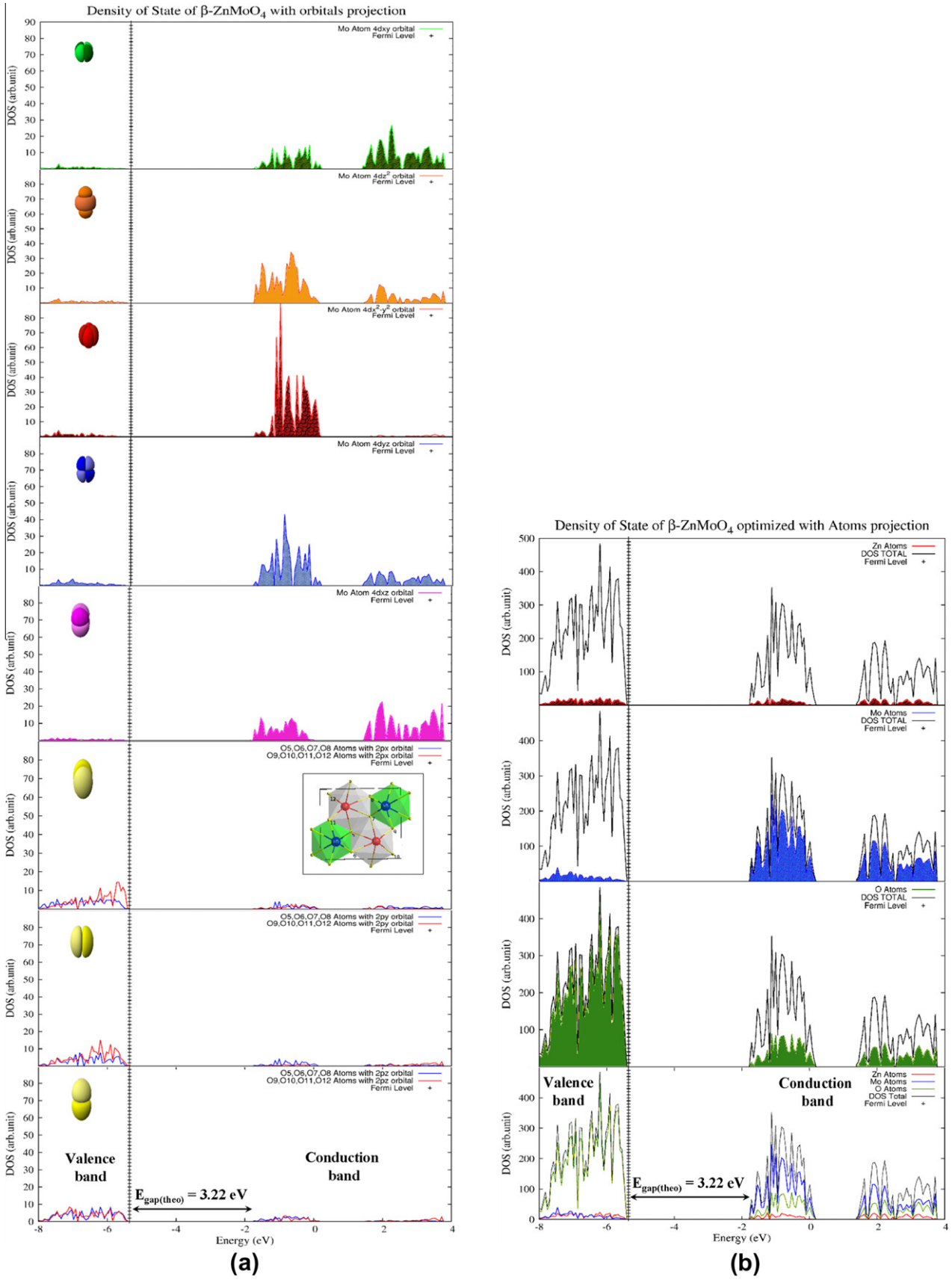


**Fig. 6.** Projected partial DOS on the Mo and O orbitals and (b) projected total DOS on the Zn, Mo and O orbitals for the β-$ZnMoO_4$ crystals.

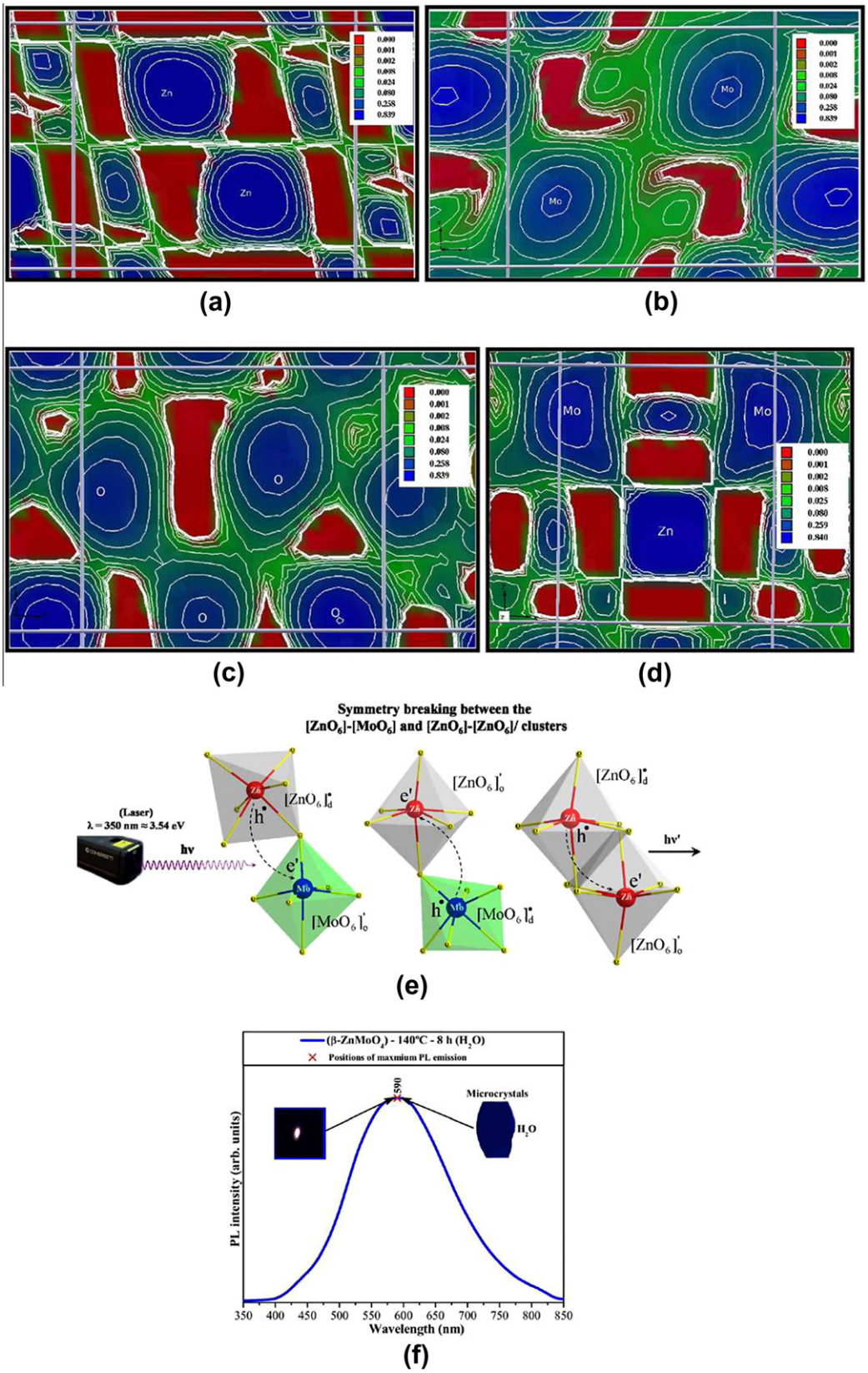


**Fig. 7.** Electronic density map on the: (a) (200) plane, (b) (100) plane, (c) (400) plane, and (d) (004) plane of the β-$ZnMoO_4$ crystals (e) Possible mechanism of charge transference between the clusters and (f) PL spectra of β-$ZnMoO_4$ microcrystals synthesized at 140 °C for 8 h in HT system. Insets show the digital photographs of its corresponding PL emissions and FE-SEM image of individual microcrystal, respectively.

electronic transitions in the band gap occur in the same region of the Brillouin zone between the maximum-energy states near to minimum-energy states (see Fig. 5(b)). During the excitation process at room temperature, some electrons localized at lower intermediary energy levels (O 2*p* orbitals) near the VB absorb photon energies ($h\nu$). As a consequence of this phenomenon, the energetic

electrons are promoted to higher intermediary energy levels (Mo 4*d* orbitals) located near the CB (see Fig. 6(b)). When the electrons revert to lower energy states, (again via radiative return processes), energies arising from this electronic transition are converted to photons ($h\nu'$) (see Fig. 7(e)). Moreover, the Fig. 7(e) shows our proposed model of electron transfer between clusters to origin PL emission of β-$ZnMoO_4$ crystals. In this model, we can attributed the possible process of charge transfer between the $[ZnO_6]_d^x$–$[MoO_6]_o^x$, $[MoO_6]_d^x$–$[ZnO_6]_o^x$ or $[ZnO_6]_d^x$–$[ZnO_6]_o^x$ clusters in the monoclinic lattice of β-$ZnMoO_4$ crystals due to order-disorder effects between clusters caused by a constant process of charge transfer according to Eqs. (9)–(11):

$$[ZnO_6]_d^x \xrightarrow{e'} [MoO_6]_o^x \Rightarrow [ZnO_6]_d^{\cdot} - [MoO_6]_o' \quad (9)$$

$$[MoO_6]_d^x \xrightarrow{e'} [ZnO_6]_o^x \Rightarrow [MoO_6]_d^{\cdot} - [ZnO_6]_o' \quad (10)$$

$$[ZnO_6]_d^x \xrightarrow{e'} [ZnO_6]_o^x \Rightarrow [ZnO_6]_d^{\cdot} - [ZnO_6]_o' \quad (11)$$

In these equations, the cluster-to-cluster charge-transfer (CCCT) in a crystal containing more than one kind of cluster is characterized by excitations involving electronic transitions from one cluster to another cluster [77]. Gracia et al. [78] have demonstrated that the CCCT mechanism in $CaWO_4$ crystals at excited states (excited singlet and excited triplet) can be considered a new class of electronic transitions which are involved in PL emissions. In this work, we consider that within the β-$ZnMoO_4$ lattice, the octahedral $[ZnO_6]$-$_d{}^x$–$[MoO_6]_o^x$, $[MoO_6]_d^x$–$[ZnO_6]_o^x$ or $[ZnO_6]_d^x$–$[ZnO_6]_o^x$ clusters (*o* = ordered and *d* = disordered/distorted) clusters arise from structural distortions in a monoclinic structure where the occurrence of electronic transference between them is possible. Therefore, several photons ($h\nu'$) originating from the participation of different energy states during electronic transitions between the VB and CB of β-$ZnMoO_4$ crystals are responsible by their broad PL properties (see Fig. 7(f)).

## 4. Conclusions

In summary, β-$ZnMoO_4$ microcrystals were synthesized successfully by the conventional HT method at 140 °C for 8 h. XRD patterns and Rietveld refinement data demonstrate that β-$ZnMoO_4$ microcrystals are monophasic with a wolframite-type monoclinic structure and space group $P2/c$. FT-Raman and FT-IR spectroscopies have been employed to verify the vibrational modes while UV–Vis absorption spectroscopy and PL measurements was used to investigate their optical properties. The experimental Raman and infrared modes are in good agreement with theoretical results. UV–Vis absorption spectra showed an optical band gap which are associated with the presence of intermediary energy levels between the VB and CB. The band structure reveals a direct band gap from Y to Y point for β-$ZnMoO_4$ microcrystals. According to the DOS analyses, the energy states in the VB is constituted main from O ($2p_x$, $2p_y$, and $2p_z$) orbitals, while in the CB there is the contribution main from Mo ($4d_{xy}$, $4d_{xz}$ and $4d_{yz}$, $4d_{x^2-z^2}$ and $4d_{z^2}$), respectively. An electron density map shows an inhomogeneous electronic distribution of charges between distorted octahedral $[MoO_6]$ and $[ZnO_6]$ clusters. The PL behavior of β-$ZnMoO_4$ microcrystals is associated with distortion effects on the octahedral $[ZnO_6]$ and $[MoO_6]$ into the monoclinic structure.

## Acknowledgements

The authors thank the financial support Brazilian Research Financing Institutions: CNPq-DCR (350711/2012-7), FAPESP (No. 2009/50303-4), CNPq-GERATEC ((555684/2009-1)), and CAPES.

## Appendix A. Supplementary data

Supplementary data associated with this article can be found, in the online version, at http://dx.doi.org/10.1016/j.poly.2013.02.006.

## References

[1] S.C. Abrahams, J. Chem. Phys. 46 (1967) 2052.
[2] Y. Li, G. Weisheng, B. Bo, G. Kaijie, IEEE Int. Conf. Energy Environ. Technol. 3 (2009) 672.
[3] G. Zhang, S. Yu, Y. Yang, W. Jiang, S. Zhang, B. Huang, J. Crys. Growth 312 (2010) 1866.
[4] W. Reichelt, T. Weber, T. Söhnel, S. Däbritz, Z. Anorg. Allg. Chem. 626 (2000) 2020.
[5] T. Söhnel, W. Reichelt, H. Oppermann, Hj. Mattauch, A. Simon, Z. Anorg. Allg. Chem. 622 (1996) 1274.
[6] K. Pavani, A. Ramanan, Eur. J. Inorg. Chem. 2005 (2005) 3080.
[7] D. Spassky, A. Vasilev, I. Kamenskikh, V. Kolobanov, V. Mikhailin, A. Savon, L. Ivleva, I. Voronina, L. Berezovskaya, Phys. Status Solidi A 206 (2009) 1579.
[8] T.N. Nikolaenko, Y.A. Hizhnyi, S.G. Nedilko, J. Lumin. 128 (2008) 807.
[9] L.I. Ivleva, I.S. Voronina, L.Y. Berezovskaya, P.A. Lykov, V.V. Osiko, L.D. Iskhakova, Crystallogr. Rep. 53 (2008) 1087.
[10] X. Ju, X. Li, W. Li, W. Yang, C. Tao, Mater. Lett. 65 (2011) 2642.
[11] L. Yu, M. Nagami, Mater. Lett. 64 (2010) 1644.
[12] A. Xei, X. Yuan, F. Wang, Y. Shi, Z. Mu, J. Phys. D Appl. Phys. 43 (2010) 055101.
[13] Z. Chunlei, H. Yunsheng, Z. Weidong, H. Xiaowei, J. Rare Earths 27 (2009) 758.
[14] L.Y. Zhou, J.S. Wei, F.Z. Gong, J.L. Huang, L.H. Yi, J. Solid. State. Chem. 181 (2008) 1337.
[15] A. Kumar, J. Kumar, J. Mater. Chem. 21 (2011) 3788.
[16] V.B. Mikhailik, H. Kraus, D. Wahl, H. Ehrenberg, M.S. Mykhaylyk, Nucl. Instrum. Methods Phys. Res., Sect. A 562 (2006) 513.
[17] C. Arnaboldi, C. Brofferio, O. Cremonesi, L. Gironi, M. Pavan, G. Pessina, S. Pirro, E. Previtali, Astropart. Phys. 34 (2011) 797.
[18] L. Gironi, C. Arnaboldi, J.W. Beeman, O. Cremonesi, F.A. Danevich, V.Y. Degoda, L.I. Ivleva, L.L. Nagornaya, M. Pavan, G. Pessina, S. Pirro, V.I. Tretyak, J. Tupitsyna, J. Instrum. 5 (2010) P11007.
[19] L.L. Nagornaya, F.A. Danevich, A.M. Dubovik, B.V. Grinyov, S. Henry, V. Kapustyanyk, H. Kraus, D.V. Poda, V.M. Kudovbenko, V.B. Mikhailik, M. Panasyuk, O.G. Polischuk, V. Rudyk, V. Tsybulskyi, I.A. Tupitsyna, Y.Y. Vostretsov, IEEE. Trans. Nucl. Sci. 56 (2009) 2513.
[20] J. Guo, D. Zhou, H. Wang, X. Yao, J. Alloys Compd. 509 (2011) 5863.
[21] B.D. Amo, R. Ramagnoli, V.F. Vetetre, J. Appl. Electrochem. 29 (1999) 1401.
[22] N.N. Leyzerovich, K.G. Bramnik, T. Buhrmester, H. Ehrenberg, H. Fuess, J. Power. Sour. 127 (2004) 76.
[23] C.C. Chen, Y.R. Jiang, K.H. Chang, Adv. Mater. Res. 557 (2012) 761.
[24] L. Lv, W. Tong, Y. Zhang, Y. Su, X. Wang, J. Nanosci. Nanotechnol. 11 (2011) 9506.
[25] A.M.E.S. Raj, C. Mallika, K. Swaminathan, O.M. Sreedharan, K.S. Nagaraja, Sens. Actuators B. Chem. 81 (2002) 229.
[26] N. Sotani, T. Suzuki, K. Nakamura, K. Eda, S. Hasegawa, J. Mater. Sci. 36 (2001) 703.
[27] A.L. Kruglyashov, E.M. Skou, Solid State Ionics 28 (1988) 233.
[28] A. Manthiram, J. Gopalakrishnan, Mater. Res. Bull. 15 (1980) 207.
[29] AM. Dubovik, Y.Y. Vostretsov, B.V. Grinyov, F.A. Danevich, H. Kraus, L.L. Nagornaya, V.B. Mikhailik, I.A. Tupitsyna, Acta Phys. Pol. A 117 (2010) 15.
[30] C.V. Bhuvana, B. Viswanathan, M.V.C. Sastri, Indian J. Chem. 1A (1979) 385.
[31] A. Sen, P. Pramanik, Mater. Lett. 50 (2001) 287.
[32] C. Peng, L. Gao, S. Yang, J. Sun, Chem. Commun. 43 (2008) 5601.
[33] J.H. Ryu, S.M. Koo, J.W. Yoon, C.S. Lim, K.B. Shim, Mater. Lett. 60 (2006) 1702.
[34] R.P. Jia, Y.Q. Zhang, J. Nanopart. Res. 12 (2010) 2717.
[35] G. Tian, Y. Chen, W. Zhou, K. Pan, Y. Dong, C. Tian, H. Fu, J. Mater. Chem. 21 (2011) 887.
[36] M. Hashim, C. Hu, Y. Chen, C. Zhang, Y. Xi, J. Xu, Phys. Status Solidi A 208 (2011) 1937.
[37] J.C. Sczancoski, M.D.R. Bomio, L.S. Cavalcante, M.R. Joya, P.S. Pizani, J.A. Varela, E. Longo, M.S. Li, J.A. Andres, J. Phys. Chem. C 113 (2009) 5812.
[38] X. Cui, S.H. Yu, L. Li, L. Biao, H. Li, M. Mo, X.M. Liu, Chem. Eur. J. 10 (2004) 218.
[39] L.S. Cavalcante, J.C. Sczancoski, M. Siu Li, E. Longo, J.A. Varela, Colloid Surf. A 396 (2012) 346.
[40] R. Jia, C. Zhang, J. Xu, Adv. Mater. Res. 624 (2012) 51.
[41] L. Wei, L. Xuan, W. Li, L. Xin, Chin. J. Lumin. 33 (2012) 1283.
[42] D.A. Spassky, A.N. Vasilev, I.A. Kamenskikh, V.V. Mikhailin, A.E. Savon, Y.A. Hizhnyi, S.G. Nedilko, P.A. Lykov, J. Phys. Condens. Matter. 23 (2011) 365501.
[43] R. Dovesi, V.R. Saunders, C. Roetti, R. Orlando, C.M. Zicovich-Wilson, F. Pascale, B. Civalleri, K. Doll, N.M. Harrison, I.J. Bush, P. D'Arco, M. Llunell, CRYSTAL09, User's Manual, University of Torino, Torino, 2009.
[44] A.D. Becke, J. Chem. Phys. 98 (1993) 5648.
[45] C. Lee, R.G. Yang, R.G. Parr, Phys. Rev. B 37 (1988) 785.
[46] Available at: <http://www.crystal.unito.it/Basis_Sets/Ptable.html>.
[47] P.J. Hay, W.R. Wadt, J. Chem. Phys. 82 (1985) 270.
[48] A. Kokalj, J. Mol. Graphics 17 (1999) 176.
[49] J. Meullemeestre, E. Penigault, Bull. Soc. Chim. France 10 (1972) 3669.
[50] H.M. Rietveld, Acta Cryst. 2 (1967) 65.
[51] Available at: <http://www.ing.unitn.it/ maud/>.

[52] L. Lutterotti, S. Matthies, H.R. Wenk, A.J. Schultz, J.J. Richardson, J. Appl. Phys. 81 (1997) 594.
[53] K. Momma, F. Izumi, J. Appl. Crystallogr. 44 (2011) 1272.
[54] Available at: <http://en.wikipedia.org/wiki/Octahedron>.
[55] L.S. Cavalcante, J.C. Sczancoski, R.L. Tranquilin, J.A. Varela, E. Longo, M.O. Orlandi, Particuology 7 (2009) 353.
[56] M. Crane, R.L. Frost, P.A. Williams, J.T. Kloprogge, J. Raman Spectrosc. 33 (2002) 62.
[57] R.L. Frost, L. Duong, M. Weier, Spectrochim. Acta, Part A 60 (2004) 1853.
[58] L.H. Hoang, N.T.M. Hien, W.S. Choi, Y.S. Lee, K. Taniguchi, T. Arima, S. Yoon, X.B. Chen, I.S. Yang, J. Raman Spectrosc. 41 (2010) 1005.
[59] T.T. Basiev, A. Ya Karasik, A.A. Sobol, D.S. Chunaev, V.E. Shukshin, Quant. Electron. 41 (2011) 370.
[60] Y. Liu, H. Wang, G. Chen, Y.D. Zhou, Y. Gu, B.Q. Hu, J. Appl. Phys. 64 (1988) 4651.
[61] M.A.P. Almeida, L.S. Cavalcante, M. Siu Li, J.A. Varela, E. Longo, J. Inorg. Organomet. Polym. 22 (2012) 264.
[62] M. Markova-Velichkova, R. Iordanova, Y. Dimitriev, Phys. Status Solidi C 8 (2011) 3159.
[63] N.M. Hung, L.T. Hang, N.V. Khanh, D.T.X. Thao, N.V. Minh, J. Nonlin. Opt. Phys. Mater. 21 (No. 1) (2012) 1250002.
[64] V.V. Fomichev, I. Kondratov, Spectrochim. Acta. 50A (1994) 1113.
[65] P. Siriwong, T. Thongtem, A. Phuruangrat, S. Thongtem, CrystEngComm. 13 (2011) 1564.
[66] Y. Keereeta, T. Thongtem, S. Thongtem, J. Alloys Compd. 509 (2011) 6689.
[67] M.R.D. Bomio, L.S. Cavalcante, M.A.P. Almeida, R.L. Tranquilin, N.C. Batista, P.S. Pizani, M. Siu Li, J. Andres, E. Longo, Polyhedron. 50 (2013) 532.
[68] K.M. Garadkar, A. Ghule, K.B. Sapnar, S.D. Dhole, Mater. Res. Bull. 48 (2013) 1105.
[69] M. Mancheva, R. Iordanova, Y. Dimitriev, J. Alloys Compd. 509 (2011) 15.
[70] P. Kubelka, F. Munk-Aussig, Zeit. Fur. Tech. Physik. 12 (1931) 593.
[71] A.E. Morales, E.S. Mora, U. Pal, Rev. Mex. Fis. S. 53 (2007) 18.
[72] V.M. Longo, L.S. Cavalcante, E.C. Paris, J.C. Sczancoski, P.S. Pizani, M.S. Li, J. Andres, E. Longo, J.A. Varela, J. Phys. Chem. C. 115 (2011) 5207.
[73] R. Lacomba-Perales, J. Ruiz-Fuertes, D. Errandonea, D. Martınez-Garcıa, A. Segura, Eur. Phys. Lett. 83 (2008) 37002.
[74] I.L. Validzic, T.D. Savic, R.M. Krsmanovic, D.J. Jovanovic, M.M. Novakovic, M.C. Popovic, M.I. Comor, Mater. Sci. Eng. B. 177 (2012) 645.
[75] J. Ruiz-Fuertes, S. Lopez-Moreno, J. Lopez-Solano, D. Errandonea, A. Segura, R. Lacomba-Perales, A. Munoz, S. Radescu, P. Rodriguez-Hernandez, M. Gospodinov, L.L. Nagornaya, C.Y. Tu, Phys. Rev. B. 86 (2012) 125202.
[76] L.S. Cavalcante, V.M. Longo, J.C. Sczancoski, M.A.P. Almeida, A.A. Batista, J.A. Varela, M.O. Orlandi, E. Longo, M. Siu Li, CrystEngComm. 14 (2012) 853.
[77] L.S. Cavalcante, M.A.P. Almeida, W. Avansi, R.L. Tranquilin, E. Longo, N.C. Batista, V.R. Mastelaro, M. Siu Li, Inorg. Chem. 51 (2012) 10675.
[78] L. Gracia, V.M. Longo, L.S. Cavalcante, A. Beltran, W. Avansi, M.S. Li, V.R. Mastelaro, J.A. Varela, E. Longo, J. Andres, J. Appl. Phys. 110 (2011) 043501.